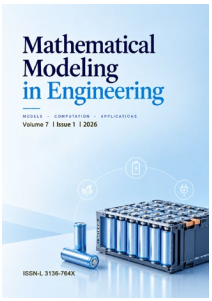
UNIVERSITY OF WEST ATTICA

eISSN: 3136-764X

Mathematical Modeling in Engineering

Vol. 7, No. 3, July, 2026



Graphormer-VAE Model for Twin Load Estimation of Hydraulic Presses Using Multiphysics Simulation and Strain Data

Milorada Vlahović[a,*], Pavlina Bogojević[a]

[a] *Faculty of Technical Sciences, University of Kragujevac, Kragujevac, 34000, Serbia*

Received 06 June 2026; Revised 26 August 2026; Accepted 04 September 2026; Published 08 September 2026

Abstract

Direct measurement of the distributed forming load in a large hydraulic press is difficult, particularly when die contact is asymmetric and frame strain is affected by temperature and support compliance. This study develops a Graphormer-VAE digital-twin estimator that combines a compact mechanical graph, multiphysics finite-element response descriptors, and sparse strain measurements to infer total vertical load and eccentric moment. Graph-biased attention encodes structural distance, edge class, and sensor centrality, while a variational latent layer provides a distribution over load states. The model was evaluated with 1,260 production-like strokes from a 20 MN four-column press, including centered loading, 60 and 120 mm lateral offsets, asymmetric die contact, and thermal-drift cases. Its mean absolute total-load error was 1.82% of rated capacity, and its eccentric-moment error was 3.7%. The corresponding errors for a graph convolutional baseline were 2.39% and 5.1%. The nominal 95% prediction interval achieved 94.1% empirical coverage, and mean inference latency was 18.6 ms per stroke window, below the 20 ms acquisition period used in this study. Removing multiphysics residual conditioning increased load error by 0.91 percentage points; removing graph-distance bias increased moment error by 1.4 percentage points. The estimator therefore links spatially sparse measurements to both load magnitude and load imbalance while expressing uncertainty. Its evidence is limited to the tested press, sensor layout, and operating cases, so transfer to other machines requires separate validation.

Keywords: Hydraulic Press Load Estimation, Graphormer VAE, Multiphysics Digital Twin, Strain Sensor Fusion, Eccentric Forming Load

1. Introduction

Large hydraulic presses are energy-intensive manufacturing facilities, and the quality of forming and structural safety depend on the load path developed among the cylinders, ram, die set, bolster and press frame [1]. The load signal available in production is often a hydraulic pressure signal, and if necessary, a small number of strain gauges can be arranged reasonably on the frame [2]. Although the above measurements can be applied to observation, they do not fully show the distribution of vertical force, eccentric moment and local bending caused by asymmetric blanks or non-uniform die contact [3]. Therefore, digital-twin modelling has been applied to press monitoring to connect a computational model of the machine with the measured status of the actual equipment [4]. Multi-physics simulations can add elastic deformation, contact stiffness, thermal drift, and boundary compliance to the combined model of the forming system, and this connection can be extended [5]. A typical problem of high-tonnage presses is that the interacting load components in a nonlinearly varying strain field due to frame flexibility, die contact and operating temperature are very

* Corresponding author: , milorada.vla@tf.kg.ac.rs

https://doi.org/10.68406/mme.2026.vol7iss3nm8:94-106

➢ This is an open access article under the CC BY-NC-SA 4.0 license (https://creativecommons.org/licenses/by/4.0/).

© Authors retain all copyrights.

difficult to reproduce. Fewer sensors and an unfavorable workshop environment are also detrimental to the observability of this inverse problem.

Most of the existing industrial load estimators are based on pressure calibration, linear regression of strain channel and total force, or finite-element lookup tables. The above methods are suitable for operation near the calibration point; however, as the die offset, change in guide friction or alteration of the neutral strain state due to thermal expansion increases, their accuracy will decline. A data-driven method has learned a non-linear mapping from multiple channels of signals to form a force based on a large amount of historical stroke data [6]. Neural surrogate models can replace repeated finite-element inversions and provide fast online estimates [7]. Many sequence networks and multilayer perceptrons treat sensor channels as an ordered input array without explicitly encoding the mechanical graph that links strain-gauge locations [8]. Graph neural networks are used to address this problem by passing information among connected structural nodes [9]. Another problem is that it cannot be known for certain; the same sparse strain pattern may be caused by friction, local contact or a change in temperature [10].

A Graphormer variational autoencoder model for twin load estimation of hydraulic presses based on Multiphysics simulation and strain data is developed in this study. The model represents the press as a mechanical graph rather than an unstructured list of channels; its specific contribution is the joint use of graph-biased attention, simulation-residual conditioning, and variational load-state inference. Graphormer attention is employed to encode topological distance, sensor centrality and load-transfer direction; a variational latent layer has been added for the uncertainty of vertical load and eccentric moment. Finite Element Twin provides the simulated strain field, thermal offset and residual response descriptor, and the physical press has synchronous strain and pressure windows. Fusion is to find the total load, left-right load imbalance, front-back moment, and a confidence interval of the operating scenario using a small number of strain gauges. The framework needs to decide whether to keep it, as an even small total-load error may still hide a dangerous eccentric state if the spatial load data is not saved by the model.

To connect the engineering motivation with a reproducible estimation and verification path, the paper presents the previous work, model construction, data integration and machine-level experiments. Section 2 introduces related research on load monitoring of hydraulic presses, multi-physics digital twins, graph learning and variational estimation. Section 3 is the twin load-estimation problem, and the Graphormer-VAE architecture is introduced. Section 4 introduces the Multiphysics simulation, sensor-fusion workflow and training procedure. Section 5 is the experiment data, comparison results, ablation analysis, robustness test and engineering interpretation. Section 6 shows the main results of this paper and discusses the deficiencies and future research directions in the conclusion.

2. Related Work

2.1. Load Monitoring and Multiphysics Digital Twins

Traditionally, load monitoring of hydraulic presses has focused on pressure-force conversion and strain-based calibration for processes. Pressure signals are convenient because they are already available in the hydraulic circuit, and they also contain useful forming load information along with cylinder friction and valve dynamics and pressure ripple. Strain-based methods can directly measure the strain at the press frame and are therefore more suitable for eccentric loading; however, the relationship between strain and load changes with the location of the sensor, local stiffness, and boundary conditions [11]. Digital-twin technology can map the measured strain to a physically meaningful deformation mode in the computer model of the machine.Digital-twin-based deformation monitoring has been demonstrated in a different manufacturing setting [12]; its transfer to press-frame load estimation therefore requires an explicit load-path model. Multiphysics modelling is necessary to account for the displacement caused by thermal expansion and contact deformation at zero load after a long period of operation [13]. Therefore, a feasible twin model should consider both the response of the structure and slowly changing operating conditions simultaneously and not treat each stroke as an independent static problem. Recently, some studies have shown that the press frame can be modeled as a load-transfer system instead of a single-stiffness coefficient [14].

The main limitation of conventional twin-based inversion is the computational cost of high-fidelity finite-element models. Although a high-fidelity model can present the distribution of local strain and stress, direct online inversion is too computationally intensive for per-stroke monitoring. Surrogate models reduce the cost by learning a low-dimensional relationship between load parameters and sensor responses. Many surrogate models are trained only on simulated data, and thus, when there are unmodeled bolted joints, guide clearance or foundation compliance in the physical machine, a domain gap may occur. Hybrid Calibration Strategies reduce the error by correcting the simulation residual with measured strokes. The current work is in this hybrid direction, but it incorporates the residual into a graph-aware variational estimator so that model correction is still associated with the structural topology of the press.

2.2. Graph Learning and Variational Estimation for Inverse Mechanical Problems

Graph learning can provide a good model of mechanical systems with distributed sensors and known structural connections. In ultrasonic structural monitoring, Sun et al. [15] used graph convolution to aggregate spatial sensor information; this provides a graph-learning precedent, not direct validation for hydraulic-press loading. Hydraulic presses are even more complicated due to the extended load transfer path of the ram, tie rods, guide columns and bolster, and the important strain channels may not be close neighbors in a simplified finite-element mesh. Transformer-based graph models solve this problem by considering all nodes and retaining the structural bias in the encoding of distance, edge type, and centrality [16]. In a load-estimation scenario, this attention can learn which remote strain channels need to be considered during the interaction of an eccentric die with a frame at one end. Graphormer-style attention has thus been relatively popular, and it can perform global interaction of explicit graph descriptors without relying solely on the depth of message passing.

Variational Estimation is employed to solve inverse problems with missing data or uncertain boundary conditions. Kruse et al. [17] used a variational autoencoder inverse mapper for material-parameter estimation in a viscoelastic model; the present load-state application is a distinct inverse problem. Due to minor variations in the distribution of friction and other factors, the sizes of the forces may differ slightly; therefore, both strain vectors are assumed to be the same. Uncertainty estimation is not a supporting output; otherwise, risk-aware monitoring of the digital twin could not be conducted in the absence of sensor data. Some research has applied probabilistic learning and physics-informed loss functions to the problem of inverse problems, but fewer studies have integrated them with graph-biased attention, multi-physics residual conditioning, and sparse strain measurements in a single press-load framework [18]. Therefore, the Graphormer-VAE model in this paper has been developed.

3. Twin Load Estimation Problem and Graphormer VAE Formulation

3.1. Graph Representation of the Hydraulic Press Twin

The load estimation problem for a four-column hydraulic press is set up, and strain gauges are attached to the uprights, crown, bolster ribs and guide-column seats. At each stroke window, the estimator obtains synchronously the strain increment, ram displacement, hydraulic pressure descriptor and simulation-derived residual descriptor. The purpose is to find the total vertical force, the left-right offset force, the front-back offset force, and an uncertainty value. A graph is built to model the machine, and nodes are set up for strain sensors, virtual finite-element response points, and load-application areas. Edges are mechanically connected, symmetrical and the main load-bearing paths. A full finite-element mesh of the graph is not necessary; a compact twin graph can be used to retain the structure required for online inference. The structure of the proposed estimator is shown in the single workflow reference of Figure 1, and the strain window, Multiphysics descriptors, graph encodings, variational latent space and load decoder are connected in a closed inference chain.

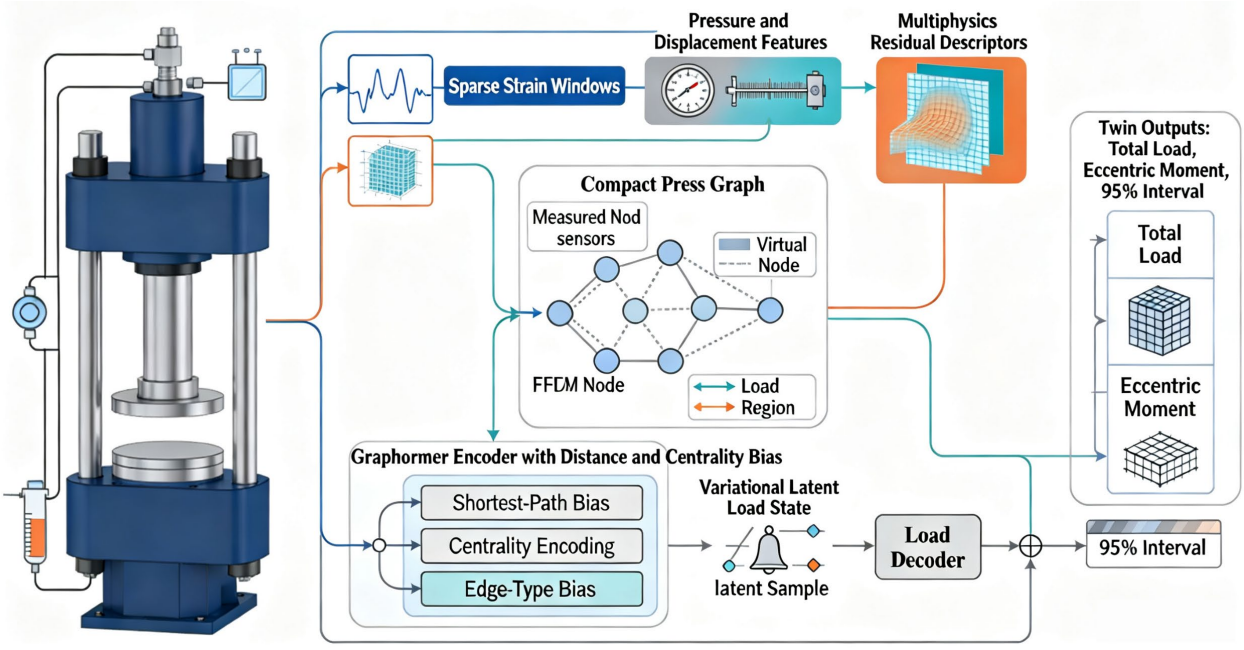


Figure 1. Graphormer-VAE twin load-estimation architecture for hydraulic press strain, simulation residual, graph bias, latent load-state inference, and uncertainty output

Let the graph be denoted as $G = (V, E)$, where V contains n measured or virtual nodes and E contains mechanical edges derived from the press structure. For node i, the input vector contains normalized strain increment, local temperature correction, simulated residual strain, pressure feature, and displacement-phase feature. The node-feature matrix is written as $X \in \mathbb{R}^{n \times d}$, and the graph-bias matrix B stores shortest-path distance, edge class, and centrality information. The load state y contains the total load and two eccentric components. The estimator learns a posterior distribution over a latent vector z rather than a single deterministic embedding.

The compact twin graph is built from three sources: the mechanical layout of the press frame, the sensor installation plan, and the finite-element response map. Measured strain gauges are retained as observed nodes, while virtual nodes are placed at the ram center, the two die-contact zones, the bolster center, and the guide-column seats.Symmetric nodes are linked by balance edges. Directed load-transfer edges follow the nominal path from die contact through the ram, columns, crown, and foundation, while edge classes distinguish these relations from sensor-to-virtual-node links. This graph construction allows the model to distinguish a uniform load increase from a lateral load migration. The graph also supports sensor dropout because virtual nodes can still aggregate information from neighboring measured nodes through the attention mechanism.

The input normalization is performed per channel and per stroke phase. For strain channel s_i at phase τ, the corrected node feature is formed by subtracting the unloaded thermal offset and adding a simulation residual descriptor. This treatment prevents the network from interpreting slow thermal drift as a mechanical load increase. The channel construction is captured by the equation below.

$$\boldsymbol{x}_i(\tau) = \left[\varepsilon_i(\tau) - \varepsilon_i^0(T), r_i^{FE}(\tau), p(\tau), u(\tau)\right] \tag{1}$$

where $\mathbf{x}_i(\tau)$ is the corrected feature vector, $\varepsilon_i(\tau)$ is the measured strain increment, $\varepsilon_i^0(T)$ is the temperature-dependent offset, $r_i^{\mathrm{FE}}(\tau)$ is the finite-element residual descriptor, $p(\tau)$ is the pressure feature, and $u(\tau)$ is the displacement-phase feature. The residual descriptor is not a replacement for measurement; it informs the estimator where the simulation expects a mismatch under a given forming phase.

3.2. Graphormer VAE Encoder and Load Decoder

The Graphormer encoder computes node interactions through attention layers enriched by mechanical graph bias. Unlike a standard transformer applied to a list of sensors, the model receives distance and edge-type information so that attention between two strain gauges reflects the mechanical relation between their mounting positions. For attention head h, the relation between nodes i and j takes the form given in the following equation.

$$a_{ij}^h = softmax_j\left(\frac{\boldsymbol{q}_i^h\left(\boldsymbol{k}_j^h\right)^{\top}}{\sqrt{d_h}} + \phi\left(D_{ij}\right) + \psi\left(C_i, C_j\right) + \eta\left(E_{ij}\right)\right) \tag{2}$$

where $\mathbf{q}_i^h$ and $\mathbf{k}_j^h$ are projected node embeddings, d_h is the head dimension, $\phi\left(D_{ij}\right)$ is a learned encoding of shortest-path distance, $\psi\left(C_i, C_j\right)$ is a centrality-pair term, and $\eta\left(E_{ij}\right)$ is an edge-type bias. These terms give the model a structural prior without preventing it from learning nonlocal load interactions.

The encoder output is pooled into a stroke-level representation h_G. Two projection heads then generate the posterior mean and variance of the latent load variable. Sampling from the learned posterior follows the equation shown next.

$$\boldsymbol{z} = \boldsymbol{\mu}_z(h_G) + \boldsymbol{\sigma}_z(h_G) \odot \boldsymbol{\epsilon}, \boldsymbol{\epsilon} \sim \mathcal{N}(\mathbf{0}, \boldsymbol{I}) \tag{3}$$

where $\boldsymbol{\mu}_z$ and $\boldsymbol{\sigma}_z$ are learned posterior parameters and $\boldsymbol{\epsilon}$ is a standard normal noise vector. The decoder maps $\mathbf{z}$ and the phase descriptor to the estimated load state. During inference, the posterior mean provides the point estimate and the posterior variance contributes to the prediction interval. The model is trained by minimizing a supervised reconstruction loss, a Kullback-Leibler regularizer, and a physics-consistency penalty between decoded load and simulated strain response. These three terms are combined in the objective equation below.

$$\mathcal{L} = \mathcal{L}_{load}(\boldsymbol{y}, \hat{\boldsymbol{y}}) + \beta D_{KL}[q_\theta(\boldsymbol{z} \mid X, B) \| p(\boldsymbol{z})] + \lambda \mathcal{L}_{phy}(\hat{\boldsymbol{y}}, X_{FE}) \tag{4}$$

where $\mathcal{L}_{\mathrm{load}}$ is the weighted error of vertical and eccentric load components, D_{KL} keeps the latent posterior close to the prior, and $\mathcal{L}_{\mathrm{phy}}$ penalizes disagreement between reconstructed load and the finite-element response map. The weights are selected on the validation set to avoid over-regularizing the physical penalty when the simulation is biased.

4. Multiphysics Simulation and Strain Data Fusion

4.1. Simulation Campaign and Sensor Synchronization

The Multiphysics twin is built from a finite-element model of the press frame, ram, bolster, guide structures, and die-contact interface. The model includes elastic deformation, temperature-dependent strain offset, contact stiffness variation, and guide-column support compliance. Rather than using the full simulated strain field online, the workflow extracts response descriptors at the compact graph nodes. These descriptors include nominal strain sensitivity to total load, sensitivity to left-right and front-back eccentricity, thermal correction, and residual deviation after calibration. The complete data-fusion procedure is referenced once in Figure 2, which links finite-element simulation, press instrumentation, feature synchronization, domain calibration, model training, and online twin deployment.

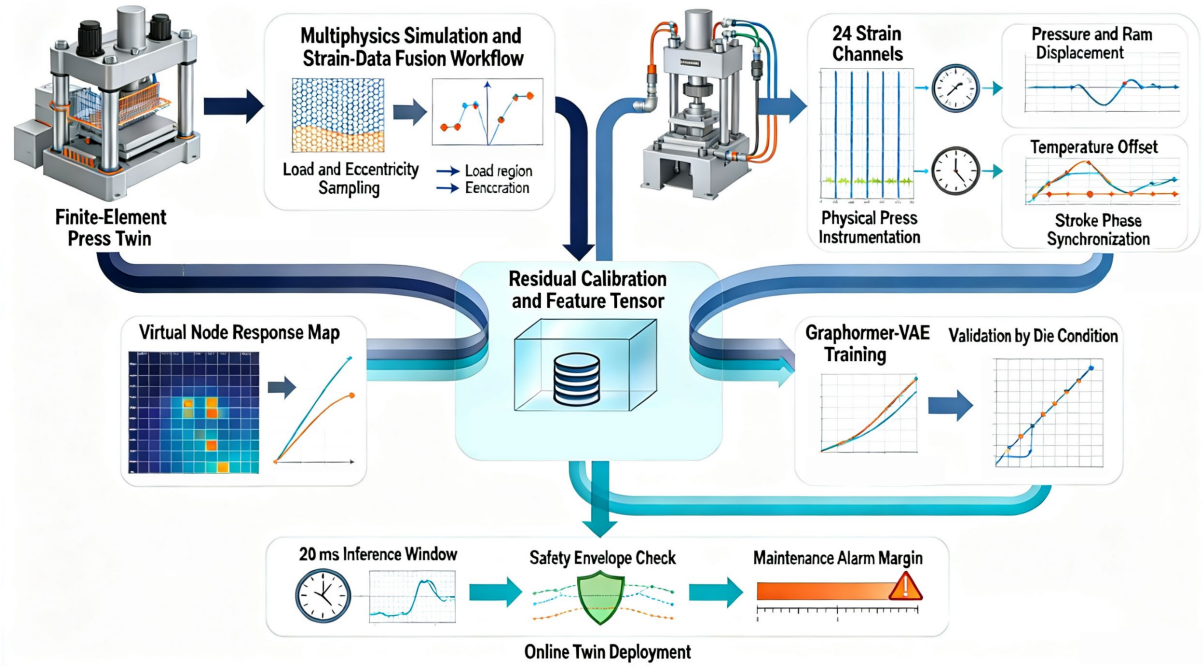


Figure 2. Multiphysics simulation and strain-data fusion workflow

Simulation cases are generated by sampling total load from 20% to 100% of nominal capacity and by varying the die eccentricity from 0 to 140 mm in both lateral directions. The thermal field is varied from 22 °C to 48 °C to emulate long production runs.Contact stiffness is perturbed within the range established during model calibration; because the numerical bounds are not reported here, the present simulation campaign should not be read as covering all tooling states. The physical data are collected from 1,260 production-like strokes, each segmented into a loading, dwell, and unloading phase. A phase-normalized representation is used because different stroke speeds produce different time lengths even when the mechanical path is similar.

The simulation campaign produces a response tensor that maps load parameters to strain descriptors at measured and virtual graph nodes.To reduce the simulation-to-machine gap, each measured stroke is paired with a simulated state using the available pressure and displacement descriptors, after which the measured-minus-simulated strain residual is retained as a conditioning feature. This pairing is a calibration step and does not use an unobserved true load at runtime. This approach is more stable than replacing measured strain with simulated strain because it lets the physical sensor data remain the primary evidence.

Phase synchronization and residual fusion are described by the following equation.

$$\boldsymbol{F}_t = \Gamma(\{\boldsymbol{\varepsilon}(t), p(t), u(t), T(t)\}, L) \oplus \Delta_{FE}(\boldsymbol{y}_{FE}, G) \tag{5}$$

where $\mathbf{F}_t$ collects measured strain, pressure, displacement, thermal offset, and finite-element residual descriptors over a window of length L. The operator Γ aligns the raw sensor streams to the normalized stroke phase, and Δ_{FE} extracts the simulation residual at the same graph nodes. The synchronized tensor is then projected to node features before entering the Graphormer encoder.

Sensor synchronization also addresses transient delay between hydraulic pressure and frame strain. Cross-correlation analysis showed that strain peaks lagged pressure peaks by 8 to 16 ms depending on die condition. The synchronization step therefore uses displacement phase as the main alignment reference and treats pressure as an auxiliary channel. This design reduces false load spikes during valve transitions.

4.2. Training Objective and Deployment Workflow

The principal partition assigns 70% of complete strokes to fitting, 15% to validation, and 15% to testing; windows from the same stroke remain in one subset. Die-condition holdout is used as a separate extrapolation check, rather than being conflated with the percentage split. This distinction prevents adjacent windows from leaking across subsets. Data augmentation includes Gaussian strain noise, random sensor dropout, residual scaling, and small phase shifts. The model is optimized with AdamW using early stopping on validation load error and interval coverage.

For online deployment, the estimator receives the most recent strain-displacement window and produces a load-state estimate every 20 ms. The posterior interval is converted to an alarm margin by comparing the upper bound of eccentric moment with a user-defined safety envelope. At runtime, the posterior-mean estimate follows the equation below.

$$\hat{\boldsymbol{y}}_t = \mathbb{E}[\boldsymbol{z}_t \mid X_t, B, \boldsymbol{c}_t] = W_d g_\theta(\boldsymbol{z}_t, \boldsymbol{c}_t) + \boldsymbol{b}_d \tag{6}$$

where $\hat{\mathbf{y}}_t$ is the posterior-mean load state, W_d is the decoder matrix, g_θ is the nonlinear decoder, $\mathbf{z}_t$ is the latent variable inferred from the graph encoder, and $\mathbf{c}_t$ contains the phase and residual-conditioning variables. The same decoder also returns variance parameters used to form confidence intervals. This workflow supports real-time supervision because only compact graph features and decoder operations are needed online.

The implementation uses four Graphormer layers, eight attention heads, a 64-dimensional latent vector, and a 128-dimensional hidden representation. The model contains 1.46 million trainable parameters. Training required 42 minutes on the workstation GPU used in this study. The reported CPU inference time is hardware-specific and describes the tested 32-sample window; longer windows can exceed the 20 ms acquisition period.

5. Experimental Data and Analysis

5.1. Load Estimation Accuracy and Comparative Performance

The experimental platform is a 20 MN four-column hydraulic press equipped with 24 strain channels, two ram-displacement encoders, cylinder pressure sensors and four temperature probes near the uprights and crown. The centre of the Stroke Program is a left-right eccentric loading of 60 mm and 120 mm, respectively, and asymmetric die contact with a front-back moment occurs. Strain-field inversion studies have shown that sparse gauges should be interpreted according to the location and load-transfer function of the structure, rather than by channel index [19].

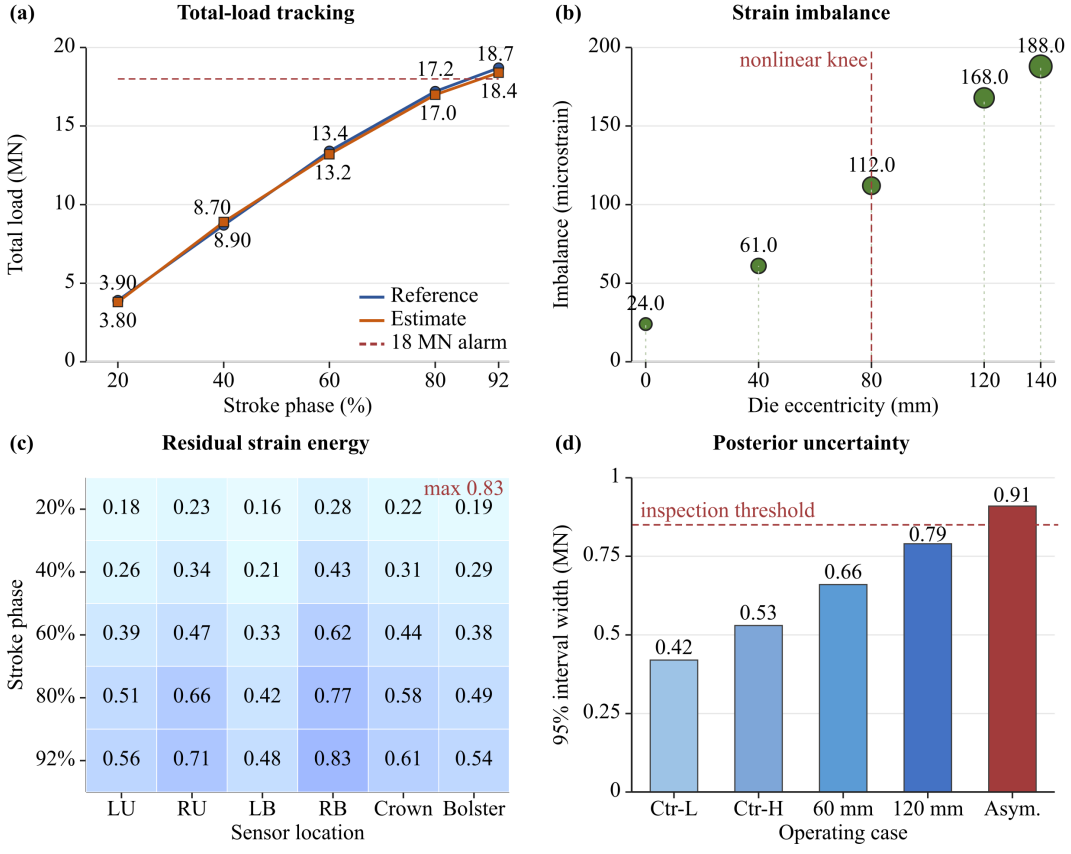


Figure 3. Measured response patterns for twin load estimation: (a) total-load tracking across stroke phases, (b) lateral strain imbalance under eccentricity, (c) residual strain-energy map, and (d) posterior interval width by operating case

As shown in Figure 3(a), the estimated total load followed the reference at 3.9 MN for the 20% stroke and increased to 18.7 MN at 92%, and the maximum absolute deviation was 0.41 MN; even after increasing the load by about five times, the deviation was still small, so the model-maintained scale consistency throughout the stroke. As shown in Figure 3(b), the imbalance of lateral strain increases monotonically with eccentricity from 24 microstrain at zero eccentricity to 188 microstrain at 140mm. A relatively larger increase in deflection per small shift of the load-center position at this location indicates that the frame is more susceptible to bending.

Figure 3(c) maps the residual strain-energy intensity by node and stroke phase. The right guide-seat node reached 0.83 at 92% phase, whereas the crown and bolster remained at 0.61 and 0.54, respectively; this spatial contrast identifies a localized contact mismatch rather than a uniform load-scaling error. Figure 3(d) shows that the 95% posterior interval width increased from 0.42 MN under centered low load to 0.91 MN under asymmetric die contact.Only the asymmetric case exceeded the 0.85 MN interval-width inspection threshold in this comparison; the threshold is an operational flag, not a physical load limit. Its wider interval indicated less certain load-path identification despite a peak total load close to the centered high-load case.

The comparison uses pressure calibration, finite-element response-surface inversion, a temporal convolutional network, and a graph convolutional network on the reported held-out cases. Total-load mean absolute errors are expressed as percentages of the press's rated 20 MN capacity. Figure 4(a) shows that mean absolute load error decreased from 5.64%, 3.48%, 2.71%, and 2.39% for these methods to 1.82% for Graphormer-VAE; the 23.8% reduction relative to graph convolution isolates the benefit of global graph-biased attention beyond local message passing. Figure 4(b) shows eccentric moment errors of 9.6%, 6.8%, 5.4%, 5.1%, and 3.7% in the same order. The larger relative gain for moment than for total load is consistent with the model's explicit encoding of long-range cross-frame relations.

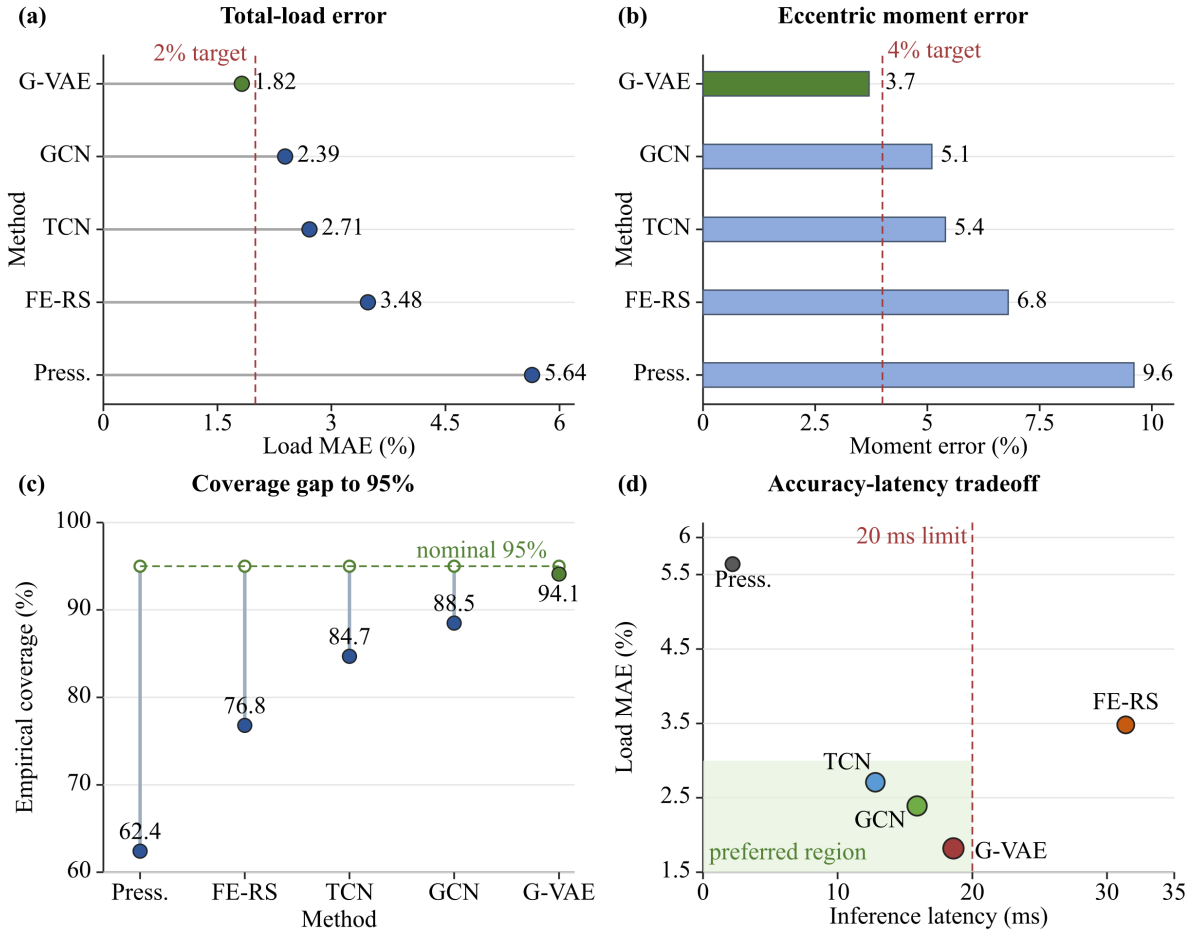


Figure 4. Comparative estimation performance: (a) total-load mean absolute error, (b) eccentric moment error, (c) prediction-interval coverage, and (d) online inference latency

Table 1 lists the operating cases used for validation. Each case contains at least 180 strokes and covers a different load-transfer condition. The asymmetric die case was intentionally retained as the hardest test condition because it combines a load-center shift with nonuniform contact timing. The measured peak load does not uniquely identify the severity of eccentricity: the centered high-load and asymmetric die cases both reached approximately 18 MN, but the latter produced more than twice the eccentric moment and a larger strain residual. Across repeated strokes, the standard deviation of peak load remained below 0.31 MN, while the asymmetric moment varied by 0.18 MN · m, providing

sufficient repeatability to compare model error without suppressing mechanically meaningful case variation. The 60 mm and 120 mm groups also preserved the expected order of lateral imbalance in more than 96% of paired strokes. Misordered pairs occurred mainly during early loading, when the absolute strain increment was less than 15% of its peak value and pressure ripple dominated the measured response. Probabilistic calibration is required when inverse estimates are compared with operational decision thresholds [20]. Figure 4(c) reports empirical coverage on the held-out evaluation samples for nominal 95% prediction intervals: 94.1% for Graphormer-VAE, 88.5% for graph convolution, and 62.4% for pressure calibration. The proposed model's coverage shortfall is 0.9 percentage points relative to the nominal level. Figure 4(d) places this reliability against computational cost. The proposed model required 18.6 ms per window, remaining 1.4 ms inside the 20 ms deployment limit, while finite-element response-surface inversion required 31.4 ms. The uncertainty layer therefore remained compatible with the controller acquisition period.

Table 1. Validation operating cases and measured load characteristics

Case	Strokes	Peak load (MN)	Eccentricity (mm)	Peak moment (MN m)	Dominant condition
Centered low load	210	9.4	0	0.21	Elastic frame response with low thermal drift
Centered high load	240	18.2	0	0.38	High vertical load with nearly balanced uprights
60 mm lateral offset	205	15.7	60	0.94	Moderate left-right moment and guide-seat bending
120 mm lateral offset	198	16.8	120	1.86	Strong eccentric moment and diagonal strain path
Asymmetric die contact	226	18.0	95	2.14	Nonuniform contact timing with front-back component
Thermal drift sequence	181	13.5	40	0.67	Long-run temperature shift and offset correction

Examine the distribution of errors in the various load regions and stroke stages. Below 8 MN, all the learning models had similar performance due to near-linear frame deformation. Above 16 MN, Graphormer-VAE had a 90th-percentile load error of 2.74% and graph convolution of 4.22%. Studies of the contact model have shown that an imperfectly identified interface stiffness can bias the inverse load recovery even after global frame stiffness calibration [21]. After changing to asymmetric loading in the current test, the response-surface error increased by 1.26 per cent; however, the learned residual branch limited this increase to 0.48 per cent. During 15%-45% stroke progress, Graphormer-VAE had a 1.54% load error, compared with 2.18% for temporal convolution and 2.91% for the response surface. During 70%-92% progress, its load and moment errors rose to 2.05% and 4.1%. The largest deviation occurred at 18.4 MN and 2.31 MN · m measured moment: the estimates were 17.9 MN and 2.17 MN · m, while the interval widened to 0.93 MN and retained the eccentric-load warning. Table 2 reports ablation results for the main architectural components. Removing graph-distance bias increased total-load error from 1.82% to 2.36% and eccentric moment error from 3.7% to 5.1%. Removing the Multiphysics residual increased load error to 2.73%, which was the largest degradation among single-component removals. Removing the variational latent layer reduced interval coverage from 94.1% to 81.6%, even though the mean load error only increased to 2.08%. The component effects were not interchangeable: graph bias mainly reduced moment error, residual conditioning mainly reduced load bias, and the variational layer preserved coverage. The full model also had a lower worst-case error than every ablation, at 6.8% versus 8.1%-10.7%.The deterministic latent replacement retained nearly the same parameter count but lost 12.5 percentage points of interval coverage. This ablation supports a role for the variational layer in calibration, although parameter count alone does not establish a causal explanation for every accuracy difference.

Table 2. Ablation study of the proposed load estimator

Model variant	Load MAE (%)	Moment error (%)	95% interval coverage (%)	Latency (*ms*)	Main effect
Full Graphormer-VAE	1.82	3.7	94.1	18.6	Balanced accuracy, uncertainty, and online speed
Without graph-distance bias	2.36	5.1	92.4	17.8	Weaker spatial load-transfer discrimination
Without multiphysics residual	2.73	5.0	91.9	17.5	Larger simulation-to-machine domain gap
Without variational layer	2.08	4.2	81.6	16.9	Poor uncertainty calibration under sparse evidence
Without sensor dropout training	2.29	4.8	89.3	18.2	Less stable under missing strain channels

5.2. Ablation Analysis and Robustness Under Sensor Disturbance

Robustness was evaluated by adding strain noise, dropping sensor channels, shifting the thermal offset, and combining these disturbances on the tested cases. As shown in Figure 5(a), the load error increased from 1.82% under

the nominal condition to 2.44% at a standard deviation of 3.0 microstrain; the increase remained below 0.16 percentage points per added microstrain up to a 1.0 microstrain noise level, after which the error rose more steeply in the tested range. The median error increased less than the 90th percentile; it rose from 2.74% to 4.06%, and the addition of noise mainly extended the difficult tail. Figure 5(b) shows that the random loss of four strain channels increased the moment error from 3.7% to 5.8%, and the simultaneous 31% expansion of the posterior interval width indicated reduced evidence rather than unchanged confidence. As shown in Figure 5(c), the predicted 90% interval covered 89.2% of the nominal samples and 86.7% under combined noise and dropout; thus, the disturbance mainly affected the calibration at the higher probability levels.

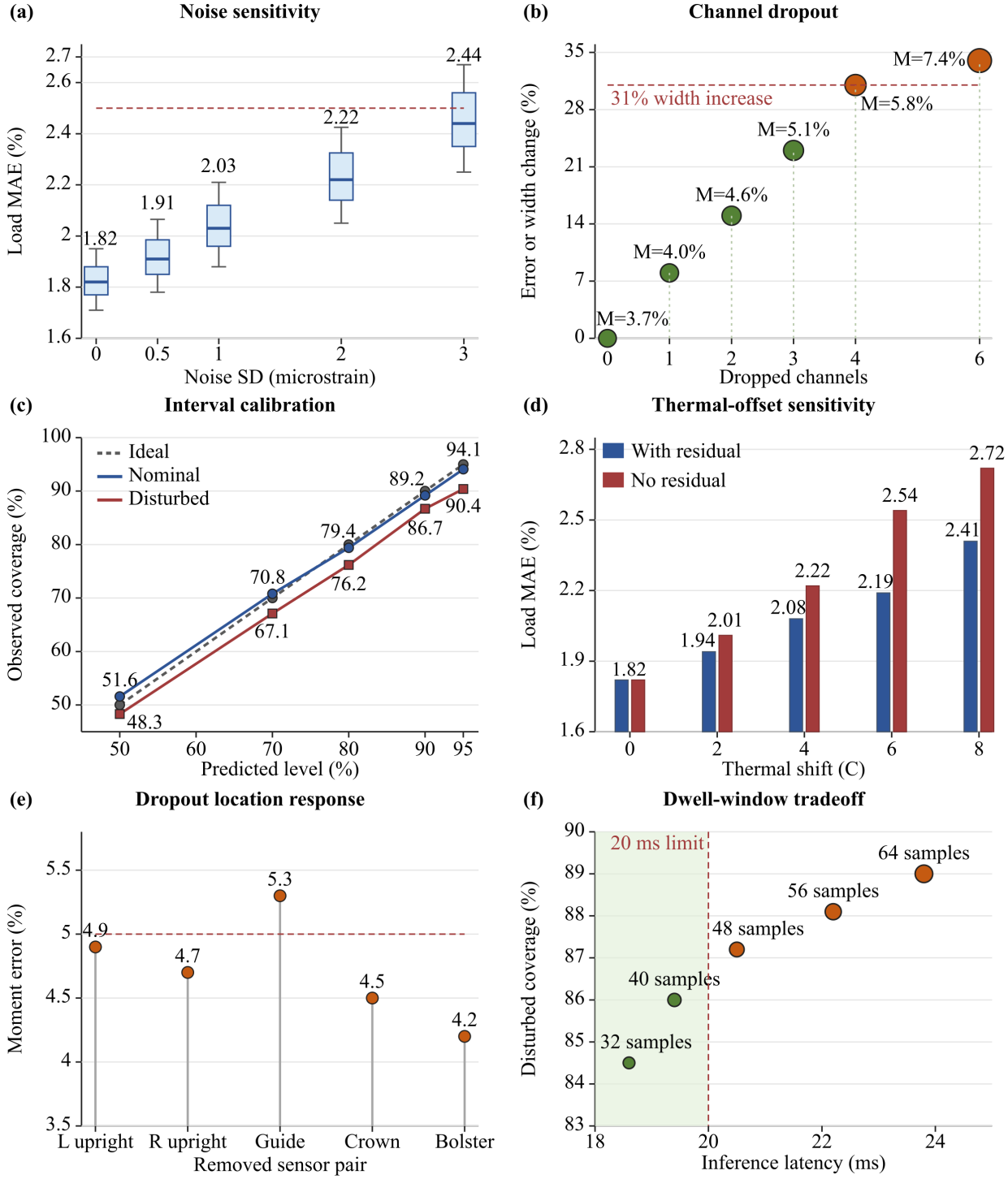


Figure 5. Robustness under disturbed sensing conditions: (a) load error versus strain noise, (b) moment error and interval expansion under channel dropout, (c) prediction-interval calibration, (d) thermal-offset sensitivity, (e) location-specific dropout response, and (f) dwell-window coverage and latency

Online twin correction is more reliable when measurement drift is separated from structural response [22]. Figure 5(d) shows that a 6 °C thermal-offset shift raised load error by 0.37 percentage points with residual conditioning,

compared with 0.72 points when the residual branch was disabled. Figure 5(e) resolves the dropout effect by location: removing a left-upright pair produced a 4.9% moment error, guide-seat loss produced 5.3%, and crown-pair loss produced 4.5%. The guide-seat penalty was largest because those channels carried opposite-sign bending information that could not be reconstructed from pressure. A deterministic estimator can remain overconfident when informative channels disappear [23]; here, the interval response increased most strongly for the same guide-seat failure.

Figure 5(f) exposes the latency-coverage tradeoff during dwell. Extending the window from 32 to 64 samples increased disturbed-case coverage from 84.5% to 89.0%, but latency rose from 18.6 to 23.8 ms and crossed the 20 ms online limit at 48 samples. A 40-sample window recovered 1.5 coverage points while using 97% of the latency budget, making it the selected fixed setting for the tested controller, subject to its limited remaining latency margin. Under simultaneous 3.0 microstrain noise, four-channel dropout, and 6 °C thermal mismatch, the eccentric moment error reached 7.2%, with 71% of the largest residuals occurring between 72% and 86% stroke phase. The nearly stationary strain field in this interval reduced temporal contrast, while the longer window recovered evidence too late for the current controller period.

5.3. Engineering Interpretation of Attention and Load State

Engineering Interpretation is shown as a single combined load-state map in Figure 6, and the five operating cases of normalized attention asymmetry, latent separation, moment utilization, interval width and tracking error are compared. Attention visualization can show which sensors are relatively more important, but based solely on this information, we should not assume a cause-and-effect relationship with the actual mechanical structure [24]. In the central case, the attention asymmetry is 12%, and the safety margin utilization is 18%. At an eccentricity of 120mm, these values were 58% and 69%, and the asymmetry of die contact reached 71% attention asymmetry and 78% moment utilization.These changes show an association between attention allocation and the imposed load path in the tested cases; attention weights alone do not establish mechanical causation.

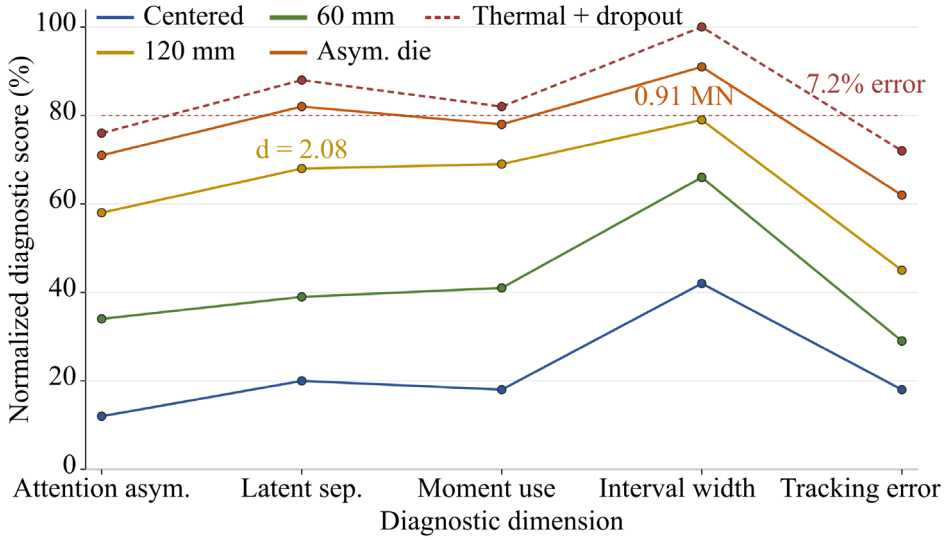


Figure 6. Integrated engineering interpretation map across operating cases, combining attention asymmetry, latent separation, moment-envelope utilization, posterior interval width, and tracking error

Latent-space geometry can describe separation among inverse states, although evidence from another inverse problem does not establish press-load identifiability by itself [25]. As shown in the combined diagram, the Mahalanobis distances between the center and 60mm eccentric stroke groups and the 120mm eccentric and asymmetric groups are 1.36 and 2.08, respectively; however, the peak loads of these two groups are similar. The five largest concentrated load attention weights are located on finite element nodes where the vertical load sensitivity is greater than 0.72 times the maximum value. Under 120 mm of eccentric load, only three out of the five high-attention nodes were relatively more sensitive to local strain; the other two were cross-frame guide-seat nodes and had a lower amplitude but a larger sensitivity to the sign of the moment. Therefore, the bias of the graph combined with the strain magnitude was found.

Risk-based monitoring frameworks adjust alarm margins according to the prediction uncertainty when measurement evidence is weak [26]. Set the safety-envelope threshold at 80% of the allowable eccentric moment, and after pressure calibration, 14 false-negative windows were obtained in the asymmetric die case; Graphormer-VAE only produced 2. Windows with an interval width of more than 0.85 MN were selected for inspection and not immediately closed. The width of the interval in the asymmetric case was 0.91 MN and the peak moment deviation was 0.62 MN·m; however, the upper posterior bound crossed the alarm threshold 36 ms before the measured peak moment occurred. This timing describes an alarm lead, whereas moment magnitude is reported separately in MN m.

Cooperative monitoring of machine and structure shows that the residual error is relatively large during rapid changes in contact conditions during calibration [27]. Fast surrogate inference is thus used to avoid repeated finite-element calculations in online supervision [28]. According to the current data, 63% of the residuals exceeding the 95th percentile occurred during dwell or asymmetric contact, and the worst-case scenario combined a 6°C thermal mismatch with guide-seat dropout. The interval width was 1.12 MN, the asymmetry of attention was 76%, and the moment utilization was 82%, but the point estimate was still 7.2% lower than that for the reference. The residual strain measured at the right rail seat is 2.6 times that at the center of the shell, while the residual strain at the crown is only 1.3 times that at the center; therefore, the issue is located near the change in the contact path. The above diagnoses will activate both the eccentric-moment alarm and the low-confidence inspection flag, and the point estimate alone cannot show the degree of the problem.

6. Conclusion

This study developed a Graphormer-VAE digital twin that combines multiphysics simulation descriptors with sparse strain measurements. On the tested hydraulic press, graph-aware probabilistic fusion estimated both total load and eccentric moment within the stated online acquisition period.

1. The proposed estimator achieved a mean absolute total-load error of 1.82% and an eccentric-moment error of 3.7%. Its nominal 95% prediction interval attained 94.1% empirical coverage, while the average inference time was 18.6 ms per stroke window, remaining within the 20 ms controller acquisition period. These results show that calibrated uncertainty can be obtained without sacrificing the response speed required for online supervision.

2. The proposed model outperformed pressure calibration, finite-element response-surface inversion, temporal convolution, and graph convolution on the reported test cases. The total-load errors of 5.64%, 3.48%, 2.71% and 2.39% for the four groups were reduced to 1.82% by Graphormer-VAE, and the corresponding eccentric-moment errors decreased from 9.6%, 6.8%, 5.4% and 5.1% to 3.7%. Ablation studies further identified the respective functions of model components: removal of graph-distance bias increased the load error to 2.36%; removal of the Multiphysics residual increased it to 2.73%; and removal of the variational layer reduced interval coverage to 81.6%.

3. The first innovation is the joint application of a compact mechanical graph, simulation-residual conditioning and variational load-state inference; however, at present, only the tested machine and sensing configuration have been applied to it. Validation was carried out on a single 20 MN press and a small number of die conditions, and the estimator needed synchronous strain and displacement signals. Under the combined disturbance of 3.0 microstrain noise, four-channel dropout and a 6 °C thermal mismatch, the eccentric-moment error reached 7.2%, and serious information loss during the dwell phase is still a significant operating limit.

The resulting framework provides a technically feasible basis for uncertainty-aware press monitoring, and future work will focus on multi-machine transfer, adaptive sensor selection, and incremental updating of the finite-element residual model under tool wear and structural aging.

7. Declarations

7.1 Author Contributions

Milorada Vlahović contributes to conceptualization, methodology, software, validation, analysis, investigation, data collection, draft preparation, manuscript editing, visualization, supervision, project administration, and funding acquisition. Pavlina Bogojević contributes to validation, analysis, investigation, data collection, draft preparation. All authors have read and agreed with the manuscript before its submission and publication.

7.2 Funding and Acknowledgments

This research received no specific financial support from any funding agency.

7.3 Institutional Review Board Statement

Not applicable.

7.4 Informed Consent Statement

Not applicable.

7.5 Date Availability

Not applicable.

7.6 Declaration of Competing Interest

The authors declare that they have no known competing financial interests or personal relationships that could have appeared to influence the work reported in this paper.

7.7 Declaration of generative AI and AI-assisted technologies

During the preparation of this manuscript, the authors utilized ChatGPT for linguistic polishing, logical organization and draft revision. The generative AI tool was not involved in research design, data collection, data analysis, or the equation of core conclusions. All outputs generated by AI were reviewed, revised and verified manually by the authors. The authors take full responsibility for all content of this manuscript.

8. References

[1] Zhang, Q., & Niu, L. (2025). Study on the upper beam of a large upsetting ratio hydraulic press frame based on ANSYS. Journal of Physics: Conference Series, 3064(1), 012037. https://doi.org/10.1088/1742-6596/3064/1/012037

[2] Peng, H., Wang, B., Ning, Y., Cao, S., & Liu, M. (2024). Strain Gauge Location Optimization for Operational Load Monitoring of an Aircraft Wing Using an Improved Correlation Measure. Applied Sciences, 14(19), 9078. https://doi.org/10.3390/app14199078

[3] Guo, H. Z., Yuen, K. V., & Mu, H. Q. (2025). Real-time Bayesian axle load estimation and structural identification of railway bridges under train loads based on strain monitoring. Engineering Structures, 322, 119195. https://doi.org/10.1016/j.engstruct.2024.119195

[4] Pantelidakis, M., & Mykoniatis, K. (2024). Extending the Digital Twin Ecosystem: A real-time Digital Twin of a LinuxCNC-controlled subtractive manufacturing machine. Journal of Manufacturing Systems, 74, 1057–1066. https://doi.org/10.1016/j.jmsy.2024.05.012

[5] Dong, Y., Zhang, P., Chen, M., & Lian, W. (2024). Numerical study of thermal contact resistance considering spots and gap conduction effects. Tribology International, 193, 109304. https://doi.org/10.1016/j.triboint.2024.109304

[6] Duan, S., Kozjek, D., Mehr, E., Anders, M., & Cao, J. (2024). Forming force prediction in double-sided incremental forming via GNN-based transfer learning. Journal of Manufacturing Processes, 120, 867–877. https://doi.org/10.1016/j.jmapro.2024.04.093

[7] Li, Q., Du, X., Ni, P., Han, Q., Xu, K., & Yuan, Z. (2024). Efficient Bayesian inference for finite element model updating with surrogate modeling techniques. Journal of Civil Structural Health Monitoring, 14(4), 997–1015. https://doi.org/10.1007/s13349-024-00768-y

[8] Fernandez-Navamuel, A., Pardo, D., Magalhães, F., Zamora-Sánchez, D., Omella, Á. J., & Garcia-Sanchez, D. (2025). Deep neural network for damage detection in Infante Dom Henrique bridge using multi-sensor data. Structural Health Monitoring, 24(1), 372–401. https://doi.org/10.1177/14759217241227455

[9] Jiang, C., & Chen, N.-Z. (2025). G-Twin: Graph neural network-based digital twin for real-time and high-fidelity structural health monitoring for offshore wind turbines. Marine Structures, 103, 103813. https://doi.org/10.1016/j.marstruc.2025.103813

[10] Jin, B., Quan, Q., & Zhang, W. (2025). Stochastic Convergence Analysis of the Inverse Potential Problem. SIAM/ASA Journal on Uncertainty Quantification, 13(3), 1334–1373. https://doi.org/10.1137/24m1703422

[11] Impraimakis, M. (2025). Deep recurrent-convolutional neural network learning and physics Kalman filtering comparison in dynamic load identification. Structural Health Monitoring, 24(3), 1752–1782. https://doi.org/10.1177/14759217241262972

[12] Yue, C., Jia, R., Zhu, X., Geng, B., & Zhang, J. (2024). Research on online deformation monitoring of thin-walled parts driven by digital twin. Digital Engineering, 3, 100023. https://doi.org/10.1016/j.dte.2024.100023

[13] Andras, A., Popescu, F. D., Radu, S. M., Pasculescu, D., Brinas, I., Radu, M. A., & Peagu, D. (2024). Numerical Simulation and Modeling of Mechano–Electro–Thermal Behavior of Electrical Contact Using COMSOL Multiphysics. Applied Sciences, 14(10), 4026. https://doi.org/10.3390/app14104026

[14] He, Z.-Q., Sami Ullah, M., & Liu, G. (2025). Load-path analysis of transverse tensile stresses in multiple-pile caps. Structural Concrete, 26(3), 3269–3281. https://doi.org/10.1002/suco.202400699

[15] Sun, L., Song, R., Wei, J., Gao, Y., Peng, C., Fan, L., Jiang, M., & Zhang, L. (2024). Physics-Augmented Spatial-Temporal graph convolutional network for damage localization using Ultrasonic guided waves. Mechanical Systems and Signal Processing, 221, 111738. https://doi.org/10.1016/j.ymssp.2024.111738

[16] Hu, T., Ma, K., & Xiao, J. (2024). Graph Feature Refinement and Fusion in Transformer for Structural Damage Detection. Sensors, 24(13), 4415. https://doi.org/10.3390/s24134415

[17] Kruse, C., Sosonkina, M., Bin Hossen, M. F., & Li, Y. (2025). Material parameter estimation for a viscoelastic stenosis model

using a variational autoencoder inverse mapper. Journal of Inverse and Ill-Posed Problems, 33(5), 617–632. https://doi.org/10.1515/jiip-2024-0048

[18] Zong, Y., Barajas-Solano, D., & Tartakovsky, A. M. (2024). Randomized physics-informed machine learning for uncertainty quantification in high-dimensional inverse problems. Journal of Computational Physics, 519, 113395. https://doi.org/10.1016/j.jcp.2024.113395

[19] Li, S., Wang, S., Cheng, Y., Peng, C., Wu, X., Zhao, J., Jiang, M., & Zhang, L. (2024). Strain/displacement field reconstruction and load identification of bracket arm structure of high-speed maglev train based on superposition conversion algorithm. Measurement, 224, 113945. https://doi.org/10.1016/j.measurement.2023.113945

[20] Xu, Y., Zheng, X., Yao, W., Zhang, X., & Xie, Y. (2025). An Improved Uncertainty Calibration Approach for Reliable Satellite Temperature Interval Prediction. Quality and Reliability Engineering International, 41(4), 1225–1234. https://doi.org/10.1002/qre.3710

[21] Fang, Z., Ma, T., Ma, Y., & Zhu, Y. (2024). Deriving stiffness indices for intelligent compaction using inverse analysis of excitation and contact forces. Automation in Construction, 166, 105637. https://doi.org/10.1016/j.autcon.2024.105637

[22] Karyofyllas, G., Giagopoulos, D., Jia, X., & Papadimitriou, C. (2026). A digital twin-driven machine learning framework for structural condition monitoring using multi-datasets. Structural Health Monitoring, 25(4), 2424–2448. https://doi.org/10.1177/14759217251324110

[23] Huang, C., Tao, C., Ji, H., & Qiu, J. (2026). Impact time history reconstruction using dynamic weighted graph neural network under sensor fault situations. Structural Health Monitoring, 25(3), 1890–1911. https://doi.org/10.1177/14759217241313177

[24] Chen, Q., & Li, B. (2025). Explainable artificial intelligence (XAI)-driven probabilistic image-based structural health monitoring of reinforced concrete beams with shear reinforcements. Automation in Construction, 180, 106549. https://doi.org/10.1016/j.autcon.2025.106549

[25] Chen, J., Jin, B., & Liu, H. (2024). Solving inverse obstacle scattering problem with latent surface representations. Inverse Problems, 40(6), 065013. https://doi.org/10.1088/1361-6420/ad466a

[26] Xu, Q., Wang, Z., Jiang, C., & Jing, Z. (2024). Data-driven predictive maintenance framework considering the multi-source information fusion and uncertainty in remaining useful life prediction. Knowledge-Based Systems, 303, 112408. https://doi.org/10.1016/j.knosys.2024.112408

[27] Khalifa, R. M., Yacout, S., Bassetto, S., & Shaban, Y. (2025). Condition monitoring and warning of a belt drive system based on a logical analysis of data regression-based residual control chart. Structural Health Monitoring, 24(3), 1657–1673. https://doi.org/10.1177/14759217241252046

[28] Schnellenbach-Held, M., Sprenger, B., & Otto, M. (2025). A Nonlinear Surrogate-Based Finite Element Model Updating Approach for Prestressed Concrete Bridges. Structural Engineering International, 35(4), 649–661. https://doi.org/10.1080/10168664.2025.2487431